Modeling the Effects of Pulse Plating on Dendrite Growth in Lithium Metal Batteries

Trevor Melsheimer¹, Madison Morey², Andrew Cannon¹, Emily Ryan^{1,2,*}

- 1. Department of Mechanical Engineering, Boston University, Boston, MA
- 2. Division of Material Science and Engineering, Boston University, Boston, MA
- *Corresponding author: ryanem@bu.edu, 617-353-7767

Abstract:

The formation of dendrites on lithium electrodes presents safety and cycling challenges for the development of high-performance, rechargeable lithium metal batteries. While a constant current (CC) charging protocol has been standard, recent studies have shown that a pulse plating (PP) charging protocol is effective at reducing dendrite growth and improving cycle life. In this study, dendrite growth at the anode-electrolyte interface was simulated using an Extended Butler-Volmer Smoothed Particle Hydrodynamics (eBV-SPH) model implemented in LAMMPS. Square waveform PP protocols were implemented and compared to CC results to understand the effect of charging protocols on lithium deposition and dendrite morphology. The charging conditions were controlled by the applied potential, as the model does not currently enforce galvanostatic conditions. Past studies compared CC and PP results at a single charging current density. In similar work on lithium-ion batteries, PP and CC results compared at the identical mean current resulted in little to no benefit to cycling performance. In this investigation, lithium anode PP protocols performed worse when compared with CC plating at the identical mean current. The PP and CC simulation results from the eBV-SPH model simulated the expected morphology and behavior found in experimental investigations and provide more detailed morphologies than previous computational simulations.

1. Introduction

The development of energy storage technologies is critical to the advancement of renewable energy, electric vehicles, and portable electronic devices. Batteries for these applications require high energy densities, fast charging, and efficient cycling. The energy capacity of current batteries is increasingly limited by the inherent theoretical energy density of the battery anode. Even state-of-the-art Lithium (Li)-ion batteries are insufficient in meeting society's future energy demand, due to the low theoretical energy density of the intercalated graphite anode [1].

Li metal batteries, which utilize a lithium metal anode, have emerged as a promising solution to the energy density challenge. The Li metal anode has a theoretical capacity (~3860 mA h g⁻¹) [2] approximately ten times greater than the traditional graphite anode used in Li-ion batteries (~372 mA h g⁻¹) [3]. While the Li metal battery shows promise, its application is hindered by severe Li dendrite growth and an unstable deposition interface [4–7]. During initial plating, the highly reactive Li undergoes secondary reactions with the organic solvent, forming a solid electrolyte interphase (SEI) at the anode surface [6,8–10]. The diffusion and reaction kinetics at the SEI layer initiate dendrite growth [9]. After initiation, the dendrites will rupture the SEI layer and continue to rapidly grow due to a lower surface resistance (i.e. a high reaction rate and fast kinetics) [9]. During the growth portion of the process preferential growth at the dendrite tips due to mass transport phenomena dominates the subsequent Li deposition [10,11]. The high curvature of a dendrite tip and its protrusion into regions of stronger electric fields results in non-linear diffusion and Li deposition [5,11]. In contrast to Li-ion batteries, where the stable SEI layer is formed during initial charging promoting higher efficiency cycling, the SEI layer within Li metal batteries in sporadically and continuously formed leading to decreased faradaic efficiency [9]. The

computational model presented in this paper simulates the preferential growth of Li dendrites and visualizes dendrite morphology, Li⁺ concentrations, and Li⁺ flux; however, this model does not directly simulate the growth of the SEI layer due to its complex nature and instead uses adjusted physical parameters such as reaction rate.

Effective methods for the suppression of dendrite growth are needed to realize the high theoretical capacity of Li metal batteries. The formation of dendrites and porous morphologies result in poor performance and safety concerns [1,12–14]. Dendrites can pierce the separator causing internal short-circuit leading to thermal runaway, capacity fade, and in extreme cases catastrophic failure [15]. Current approaches include mechanically blocking growth with solid electrolytes [16], modifying surface characteristics [17], and augmenting charging protocols [18].

Researchers have shown that, in comparison to charging with a constant current (CC), the use of different charging protocols, such as Pulse Plating (PP) [19–28] and Reverse Pulse Plating (RPP) [23,29,30] enable uniform deposition of Li. Traditional CC charging applies a constant current to the anode over a specified charging period. It is widely accepted that low current densities, which lead to reaction limited deposition, stabilize cycling and promote uniform Li deposition, and high current densities lead to diffusion limited deposition and the rapid growth of branched, needle-like dendrites [4,13,31–33]. PP is still novel for Li metal battery charging but has been extensively utilized in metal electrodeposition techniques and battery charging methods [28]. The PP charging protocol consists of a brief charge period followed by a relaxation period. The charge period utilizes a high current density (~10 mA cm⁻²) resulting in many Li dendrite nucleation sites while not depleting the Li⁺ near the anode [18]. This charge period is then followed by a longer relaxation period, where a lower current (typically zero) is applied [28,30], allowing for the Li⁺ to migrate towards the anode and minimize the concentration gradient. RPP replaces the zero applied current relaxation period with a discharging current, or anodic pulse leading to the dissolution of Li into the electrolyte near the anode [27]. Anodic pulses can then be followed by another charging period or a relaxation period. Like CC charging, both pulse charging waveforms will be repeated until a specified state of charge [23,27].

In an experimental study of PP and RPP on Li electrodeposition, Yang et al. [23] investigated dendrite growth and morphology through a series of modified Li button cell cycling tests. In their work, the researchers focused on developing different waveforms to minimize the heterogeneous deposition of Li and maximize the cycling capabilities. By varying the charge period, relaxation period, and current density the group extensively characterized the effect of duty cycle, which is the ratio of charge to cycle period, on cycling efficiency. CC charging in the diffusion limited regime (i.e. a high current density of 10 mA cm⁻²) had needle-like, branched dendrites, and poor cycling efficiencies. Meanwhile, PP waveforms comprised of short charge periods and long relaxation periods improved Li particle size, dendrite morphology, and cycling performance, when compared to CC results at the same high charging current. The researchers found that PP moderated the diffusion-controlled situation by allowing Li⁺ to replenish the diffusion layer during nucleation and tip growth. Results from recent experimental investigations have expanded on the positive benefits of PP for cycling efficiency at the same charging currents [24–26]. Aryanfar et al. have studied the optimal PP protocols for the inhibition of dendrite growth [22], the suppression of dendrite growth with RPP protocols [29], and the real-time control of dendritic propagation using adaptive PP relaxation periods [18].

Previous experiments and simulations of Li anodes studied the effect of PP relative to CC protocols at the same charging current. However, this approach does not account for the alternative case of lowering the constant current values to the PP waveform's mean current. A review of Li-

ion battery research found the mean charging current, dependent on the pulse/relaxation frequency, to be an essential benchmark for studying the performance of novel charging protocols [28]. Experimental results of PP for Li-ion batteries by Keil *et al.* [34] found little to no benefit of PP on the cycling performance of Li-ion batteries. PP studies for Li electrodeposition have demonstrated significant performance improvements at higher current densities where CC charging is severely diffusion-limited [23,25]. However, past studies of PP protocols for Li metal batteries do not directly compare results to the mean charging current [19–26], where charging times would be comparable and Li electrodeposition performance more competitive. In the recent numerical mass transport simulations of pulsed and constant plating protocols by Maraschky *et al.* [35] it was shown that PP does not provide any benefit to the microscale current distribution when compared to CC at the identical mean current. This work provided important insight on current distributions at the microscale, however the physical growth and morphology of Li dendrites under similar charging conditions was not modeled.

Computational modeling of the chemical and physical phenomena at the anode-electrolyte interface can provide insight into the effect of charging protocols on Li dendrite growth and morphology. Monte Carlo and coarse-grain (CG) models have been developed to study Li dendrite growth under varying charging protocols [19,20]. While these methods highlight the dominant phenomena in the dynamics of dendrite growth, the Monte Carlo and CG methods do not operate at realistic scales nor produce physical dendrite morphologies. The Lagrangian particle-based smoothed particle hydrodynamics (SPH) method [36–38] has been used to study dendrite growth in batteries and can simulate physically representative dendrite morphologies comparable to experimental results [39–41].

In this work, we introduce a novel application of the extended Butler-Volmer Smoothed Particle Hydrodynamics (eBV-SPH) model developed by Morey et al. [41] which simulates charging protocols and their effect on realistic dendrite growth and morphology. The eBV-SPH model does not currently enforce galvanostatic conditions. Instead of controlling charging conditions through adjustments in current, the applied potential is used to control deposition and charging protocols. For consistency regarding experimental studies, CC and PP terminology will be used throughout this work. PP and CC charging protocols are simulated using the eBV-SPH model and dendrite growth and morphology for the charging protocols are compared at identical mean current densities. The relative performance of PP and CC charging protocols at the mean current is critical for fair comparison of results [34]. The model is used to simulate square wave PP protocols cycling between charging and relaxation periods and to investigate the effect of PP charging protocols at various duty cycles on dendrite growth and morphology. Li⁺ concentration and flux are critical to understanding the physical effects of PP on the anode-electrolyte interface where dendrites form. In this work local concentrations and fluxes are calculated and used to understand how PP could improve Li metal battery performance. Dendrite morphologies are qualitatively compared to experimental results from Yang et al.'s [23] button cell charging protocol experiments.

2. Computational Methods

The SPH numerical method [36–38] is used to simulate dendrite growth at the anodeelectrolyte interface. As a Lagrangian, particle-based computational fluid dynamics method, it is well suited for moving boundaries like that of dendrite growth during the electrodeposition of Li. Simulations are run using the open-source Large-scale Atomic/Molecular Massively Parallel Simulator (LAMMPS) code base [42]. The model has been validated in previous studies on Li metal batteries [39,41] and used to study the effects of surface characteristics [41], cycling [40], electro-convection [43], battery separators [44], and anisotropic diffusion [45] on Li transport and dendrite growth and morphology. In this work, the charge-discharge cycling simulations presented in Tan *et al.* [40] have been modified to simulate square wave PP cycles. The numerical model presented is used to study the anode-electrolyte interface of Li metal batteries. This model could also be applied to other electrodeposition and dissolution processes such as other alkali or similarly reactive metals through adjustment of the physical parameters.

The simulation domain includes the anode surface, the diffusion layer in the electrolyte, and the dendrite structures (Fig. 1) with periodic boundary conditions on the left and right bounds. The concentration of cations and anions (C_i) are assumed to be initially constant ($C_{i,0}$) throughout the domain:

$$C_i(y, t = 0) = C_{i,0} \tag{1}$$

where the subscript i is the ion type, cation (c) or anion (a), and $C_{i,0}$ is the initial concentration. When a charging voltage is applied the cations (i.e. Li^+) move toward the anode surface while the anions move away from the anode. At the anode surface the Li^+ are reduced with electrons (e^-) forming Li metal on the surface. This creates a Li^+ concentration gradient and diffusion flux (Fig. 1). The reaction between Li^+ and e^- is

$$Li^+ + e^- \rightleftarrows Li \tag{2}$$

The electro-potential distribution is governed by the electrostatic (E-S) Poisson equation given by

$$\nabla^2 \emptyset(\vec{r_s}, t) = -\frac{F}{\varepsilon} \left(C_c(\vec{r_s}, t) - C_a(\vec{r_s}, t) \right), \vec{r_s} \in \Gamma, t > 0$$
 (3)

Where F is the Faraday constant and ε is the electrolyte permittivity. The reference potential is equal to the ground potential.

$$\phi(\vec{r}_s, t) = 0 \, \vec{r}_s \epsilon \Gamma, t > 0 \tag{4}$$

The Nernst-Planck (N-P) equation [46] is then solved for the change in concentration of ions in the electrolyte,

$$\frac{\partial C_i(\vec{r},t)}{\partial t} = \nabla \cdot \left(D_i(\vec{r}) \nabla C_i(\vec{r},t) \right) + \mu_i \nabla \cdot \left(C_i(\vec{r},t) \nabla \phi(\vec{r},t) \right), \vec{r} \in \Omega_F$$
 (5)

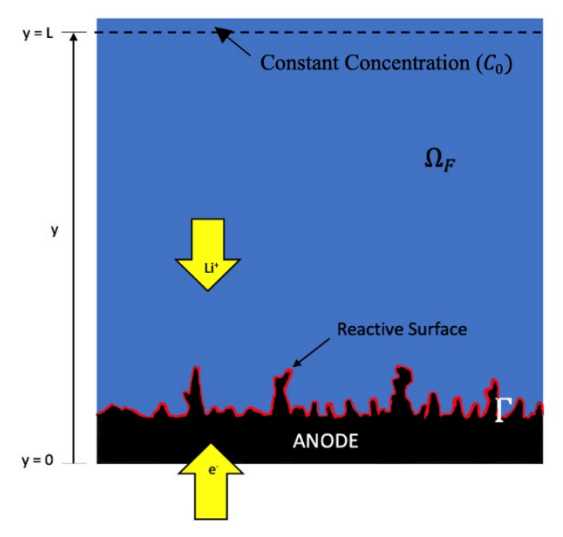


Figure 1: Schematic of the eBV-SPH LAMMPS simulation domain, where Q_F is the electrolyte.

where the first term on the right-hand side of the equation is the diffusion term with the diffusion constant, D_i , and the time dependent concentration, $C_i(\vec{r},t)$. The second term tracks the migration of ions resulting from the local potential $\nabla \emptyset$, where μ_i is the migration mobility term (assumed constant). The electrolyte fluid domain is denoted Ω_F , \vec{r} is a point in the electrolyte and the subscript i is the ion type, cation (c) or anion (a).

Outside of the electrolyte diffusion layer (L) the concentration is assumed to be constant

$$C_i(y = L, t) = C_{iL} \tag{6}$$

Where $C_{i,L}$ is the constant concentration at y=L. At the anode/electrolyte interface a reactive boundary condition is used to simulate Li⁺ deposition,

$$D_c(\vec{r})\nabla C_c(\vec{r}_s, t) + \mu_c C_c(\vec{r}_s, t)\nabla \phi(\vec{r}_s, t) = k_I, \vec{r}_s \epsilon \Gamma$$
(7)

where $\vec{r_s}$ is a point on the reactive surface (Γ) and k_J is the reaction term which includes the extended Butler-Volmer equation (eBV) and models the reduction reaction [41],

$$k_{J} = k^{0} C_{c,L}^{\alpha_{c}} C_{a,L}^{\alpha_{a}} \left[\frac{C_{c}(\vec{r},t)}{C_{c,L}} \exp\left(\frac{\alpha_{a}F}{RT}\eta\right) - \frac{C_{a}(\vec{r},t)}{C_{a,L}} \left(-\frac{\alpha_{c}F}{RT}\eta\right) \right], \vec{r}_{s} \in \Gamma, t > 0$$
 (8)

where T is the temperature, α_c and α_a are the cathodic and anodic transfer coefficients respectively, R is the ideal gas constant and k^0 is the fixed reaction rate. $C_{c,L}$ and $C_{a,L}$ are the constant concentrations in the bulk electrolyte. The overpotential, η , is given by [47]

$$\eta = \emptyset_{APP} - \emptyset_{eq} \tag{9}$$

where \emptyset_{APP} is the applied potential and \emptyset_{eq} is the equilibrium potential which is the difference between the local potential and the reference potential obtained from eq.3 and eq. 4. There is a zero-flux boundary condition for anions at the anode-electrolyte interface,

$$D_a(\vec{r})\nabla C_a(\vec{r}_s, t) + \mu_a C_a(\vec{r}_s, t)\nabla \phi(\vec{r}_s, t) = 0, \vec{r}_s \epsilon \Gamma$$
 (10)

The governing equations are implemented into the SPH model via the discretization scheme of Tartakovsky *et al.* [48] for Fickian Diffusion and precipitation, the discretization scheme of Cannon *et al.* [39] for migration, the discretization scheme of Morey *et al.* [41] for the eBV equation and the heterogenous reaction boundary condition is implemented via the continuum surface reaction (CSR) method [45]. The final forms of these equations and their implementation along with detailed verification and validation can be found in the references. The governing equations are implemented into the SPH module in the open source LAMMPS code base [42]. Table 1 presents the simulation parameters for the PP and CC simulations presented in this paper. These parameters were adopted from previous work that modeled 2D dendrite growth with the SPH methods under which the system was verified [40,43,45]. A flow chart explaining the simulation process and integration of governing equation is shown in Fig. 2.

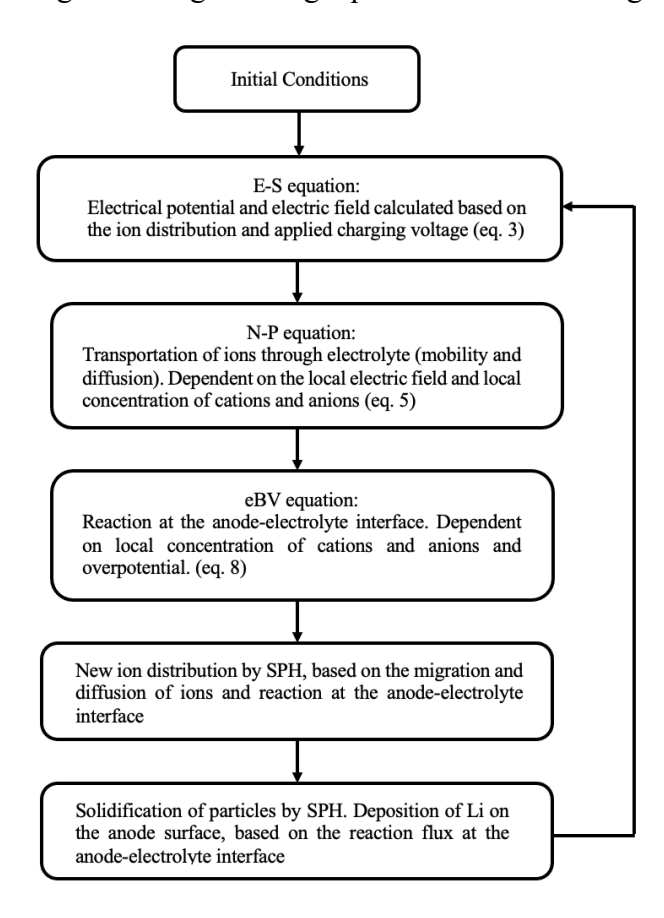


Figure 2: Flow chart of the numerical implementation of the governing equations in the eBV-SPH model.

2.1 SPH Integral Interpolant and Summation

In the SPH method, the simulation domain is divided into a finite number of particles. Each individual particle has its own properties such as mass m_a , density ρ_a , and a position r. The SPH

method uses an integral interpolant, $A_s(r)$ to approximate the property A based on the properties of its neighboring particles, [37]

$$A_{s}(r) = \int A(r')W(r - r', h)dr', \qquad (11)$$

where r is the position of the particle of interest, r is the position of neighboring particles, h is the smoothing length defining the influence area of the kernel function, and dr' is the differential volume element. The smoothing function, W, is an M₆ smoothing function given by [49]

$$W(\overrightarrow{r_{ij}},h) = \alpha \begin{cases} \left(3 - \frac{3|\overrightarrow{r_{ij}}|}{h}\right)^5 - 6\left(2 - \frac{3|\overrightarrow{r_{ij}}|}{h}\right)^5 + 15\left(1 - \frac{3|\overrightarrow{r_{ij}}|}{h}\right)^5 & 0 \le |\overrightarrow{r_{ij}}| < \frac{h}{3} \\ \left(3 - \frac{3|\overrightarrow{r_{ij}}|}{h}\right)^5 - 6\left(2 - \frac{3|\overrightarrow{r_{ij}}|}{h}\right)^5 & \frac{h}{3} \le |\overrightarrow{r_{ij}}| < \frac{2h}{3}, \\ \left(3 - \frac{3|\overrightarrow{r_{ij}}|}{h}\right)^5 & \frac{2h}{3} \le |\overrightarrow{r_{ij}}| < h \\ 0 & h < |\overrightarrow{r_{ij}}| \end{cases}$$
where $\alpha = \frac{63}{478\pi h^2}$ for two spatial dimensions.

Where $\alpha = \frac{63}{478\pi h^2}$ for two spatial dimensions.

This integral is then approximated via summation over all neighboring particles [37]. Although the summation is over all particles, the interpolating kernel vanishes at a finite distance, h, resulting in the summation over only near neighbor particles (b),

$$A_s(r) = \sum_b m_b \frac{A_b}{\rho_b} W(r - r_b, h)$$
 (13)

where ρ_b , r_b and m_b are the density, position, and mass of particle b respectively and A_b is the quantity of A at r_b .

Table 1:	Simulation	Parameters	[5.6	5.3	9-41	.43.	.451.

Parameter	Symbol	Value	Unit
Domain Length	L	5.0	μm
Domain Width	W	2.5	μm
SPH Particle Interval	Δx	0.0083	μm
Kernel Density [39]	$n_{\rm eq}$	30	particles μm ⁻²
Mobility [39]	μ	0.5	$\mu m^2 V^{-1} s^{-1}$ $\mu m^2 s^{-1}$
Diffusion Coefficient [40,43,45]	D	1.0	$\mu m^2 s^{-1}$
Initial Anion Concentration [6]	$C_{a,0}$	0.5	μ mol μ L^{-1}
Initial Cation Concentration [6]	$C_{c,0}$	0.5	$μ$ mol $μ$ L $^{-1}$
Anion Concentration (Bulk Electrolyte)	$C_{a,L}$	0.5	μ mol μ L ⁻¹
Cation Concentration (Bulk Electrolyte)	$C_{c,L}$	0.5	$μ$ mol $μ$ L $^{-1}$
Transfer Coefficients [5]	α_c , α_a	0.5	n.a.
Reaction Rate [41]	\mathbf{k}^0	$1.0x10^{-3} / n_{eq}$	$\mu m^2 s^{-1}$
Applied Potential (PP) [41]	\emptyset_{APP}	0.244	V

3. Charging Protocols

The PP charging protocol used in this study is a square waveform cycling through periods of high applied potential (charging periods) and zero applied potential (relaxation periods) (Fig. 3).

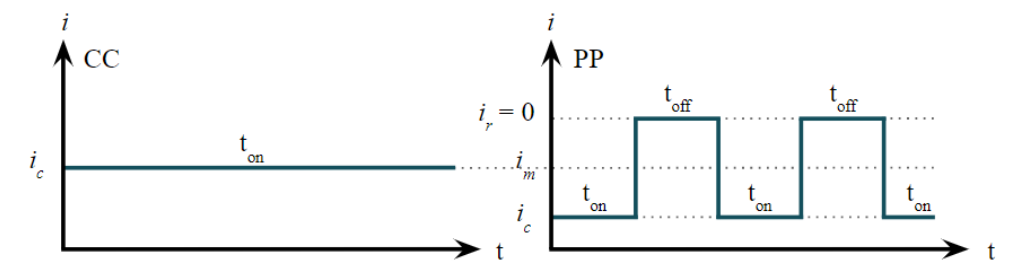


Figure 3: Schematic of constant current (CC) and pulse plating (PP) waveforms. Denoted are the charging period (t_{on}) , relaxation period (t_{off}) , relaxation current density (i_r) , charging current density (i_c) , and mean current density (i_m) .

One pulse period (P) is defined as

$$P = t_{on} + t_{off} \tag{14}$$

where t_{on} is the length of the charging period and t_{off} is the length of the relaxation period. The pulse cycle is typically represented as the PP frequency, f_{PP} , in units of hertz (Hz)

$$f_{PP} = \frac{1}{P} \tag{15}$$

And the duty cycle (D) is used to characterize the ratio of the charging period to the pulse cycle period

$$D = \frac{t_{on}}{P} = t_{on} f_{PP} \tag{16}$$

PP at a low duty cycle results in the most favorable deposition behavior, dendrite morphology, and cycling performance [18,20,23,24,28,29]. Fig. 4, which was adapted from experimental data by Zhang *et al.* [24], shows that the cycle life increases dramatically when the duty cycle is decreased from 1.0, which has no relaxation period, to a duty cycle of 0.05 which has very short charging periods followed by long relaxation periods. The shorter charging period reduces the mean current and limits non-uniform Li deposition, excessive Li⁺ depletion, and fast dendrite tip growth. Since the CC result represents the effect of a high current density of 10 mA cm⁻², it is unclear if the improvements in cycle life are due to the PP protocols or reduced mean current.

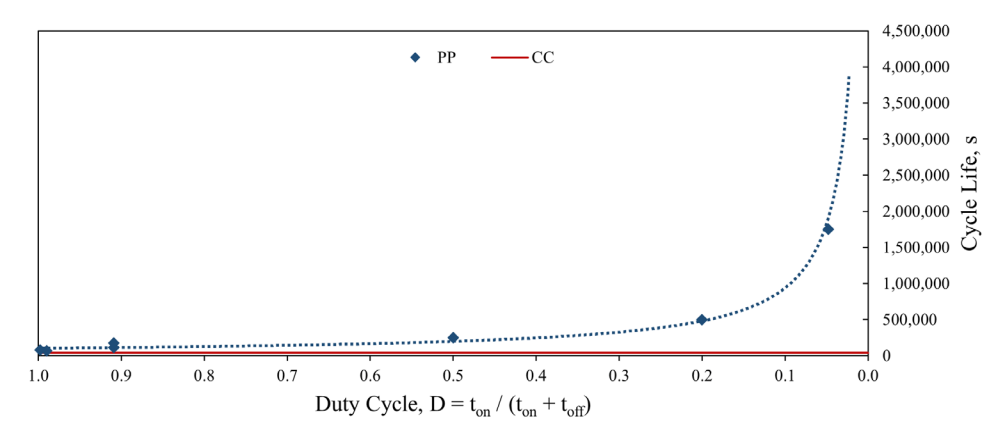


Figure 4: Experimental data from a symmetric Li/Li cell charged/discharged at 10 mA cm⁻² using CC and PP charging protocols. Cycle life increases as the duty cycle, and therefore mean current, decreases. Adapted from Supplementary Information Figure S8., Zhang *et al.* [24].

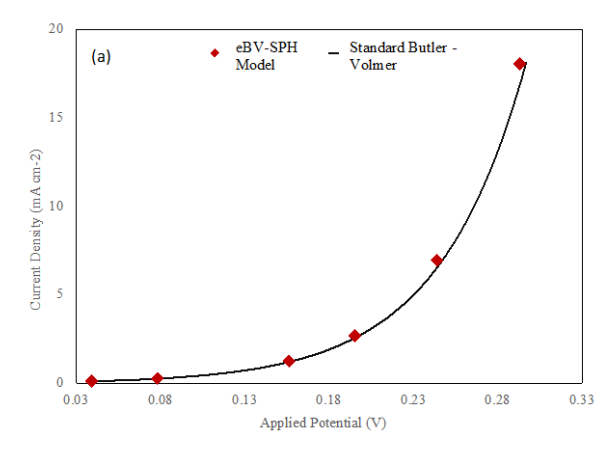


Figure 5: Comparison of eBV-SPH model to the standard BV equation used for verification of model. Adapted from Morey *et al.* [41].

In the experimental study of Li metal PP by Yang *et al.* [23], the minimum charging period was determined by the minimum duration allowed by the instrument ($t_{on} = 0.2$ ms). Longer relaxation periods are beneficial for regenerating Li⁺ concentrations; however, because results varied slightly between 5 ms and 1 s and to avoid exceptionally long test times, the relaxation period was set to $t_{off} = 5$ ms [23]. Another study selected a fixed relaxation period of $t_{off} = 5$ s under similar reasoning [26]. In this work, PP is simulated at a constant relaxation period of $t_{off} = 20$ ms. This relaxation period was selected among test cases to ensure sufficient regeneration of the depleted ions as well as computationally feasible simulation times and charging periods. Furthermore, the effect of longer relaxation periods was investigated through a range of duty cycles D = [0.09, 0.20, 0.50, 1.00] created by varying the charging period t_{on} . PP simulations are run with an applied electric field of 50 mV μ m⁻¹ resulting in an applied potential of ~0.244 V and subsequently a current density of 7.0 mA cm⁻². Fig. 5 depicts the conversion of the chosen applied potential to its equivalent current density, taken from the verification of the BV equations [41].

Since PP protocols effectively reduce the mean current, PP results are mainly compared to CC results at the identical mean current. The mean current density from PP waveforms is calculated as

$$i_m = \frac{i_c t_{on} + i_r t_{off}}{t_{on} + t_{off}} = i_c D \tag{17}$$

where i_m is the mean current, i_c is the charging current, i_r is the relaxation current, and $i_r = 0$ during PP protocols. Comparing results using the identical mean current provides a more rigorous analysis of the PP method than the commonly used method of comparing PP to CC at the charging current (i_c) . Ideally, PP would operate under a high current density that allows for fast charging. Using a high current density for CC charging would naturally lead to a faster total charging time and unfavorable needle-like dendritic growth. Results at the identical mean current (i_m) are important to study because PP and CC charging times would be similar and dendrite growth would be more competitive.

The results for PP and CC charging scenarios are compared at the same Li mass deposited (m_{max}) . A dimensionless mass fraction (M) representing the current state of deposition is defined as

$$M = \frac{m_{Li}}{m_{max}} \tag{18}$$

where m_{Li} is the mass of Li deposited on the anode surface at the current timestep and m_{max} is the mass of Li deposited on the anode surface at the end of the total charging period. The current mass (m_{Li}) is normalized by a final mass of $m_{max} = 2.20 \mu g$, chosen from the high duty cycle scenario (i.e. D = 0.5). The tabulated results are presented for M = 1.0, when $m_{Li} = m_{max}$.

To quantify the performance of the charging protocols, the density (ρ) of the simulated Li deposition is computed, in units of $\mu g \mu m^{-2}$, as

$$\rho = \frac{m_{Li}}{WL_{max}} \tag{19}$$

where W is the width of the anode in the simulation domain and L_{max} is the distance of the maximum dendrite length from the anode surface, and m_{Li} is the measured mass of Li deposited on the anode surface.

4. Results and Discussion: Effect of Pulse Plating Protocols on Dendrite Growth and Morphology

To study the effects of charging protocol and current density on dendrite growth and morphology in a Li metal battery, PP and CC charging protocols are simulated at $i_m = [0.6, 1.4, 3.5, 7.0 \text{ mA cm}^{-2}]$, where the charging current (i_c) is set to i_m for the CC cases and i_m is the mean current density at each PP duty cycle. The duty cycle for the PP simulations ranges from 0.09 to 0.5; note the 7.0 mA cm⁻² CC case corresponds to a duty cycle of 1.00. The PP cases used a high current density (i_c) of 7.0 mA cm⁻² and varied the charging time (t_{on}) to adjust the duty cycle and mean current (t_m). The mean current densities are simulated by setting corresponding applied potentials, V_{app}, in the eBV-SPH model (Fig. 5). These parameters are summarized in Table 2 for both the CC and PP cases. The experimental button cell testing of Yang *et al.* [23] used similar parameters with a range of duty cycles from 0.07 to 1.00 and charging current densities of 1 and 10 mA cm⁻².

Table 2: PP and CC simulation cases. *Taken at M = 0.79.

Case	i_m	ton	f_{PP}	Duty	V_{app}	t	ρ
	$[mA cm^{-2}]$	[ms]	[Hz]	Cycle	$[mV \mu m^{-1}]$	[s]	$[\mu g \mu m^{-2}]$
PP-1	0.6	2.0	45.5	0.09	50	16.35	0.543
PP-2	1.4	5.0	40	0.20	50	13.10	0.399
PP-3	3.5	20	25	0.50	50	7.69	0.238
CC-1	0.6	-	-	-	24	14.30	0.683
CC-2	1.4	-	-	-	34	11.25	0.379
CC-3	3.5	-	-	-	44	7.15	0.221
CC-4	7.0	-	-	1.00	50	2.68*	0.167*

Table 2 also includes the density of Li deposition (ρ) and the total charge time (t). The total charge time is defined as the time once M is equal to 1.0 ($m_{Li} = m_{max}$) as defined by Eq. 18. In the CC test at $i_m = 7.0$ mA cm⁻² ($V_{app} = 50$ mV μ m⁻¹) the total charge time is reported for M = 0.79, because the dendrite tip reached the simulation domain boundary prior to M = 1.0. This indicates that at 7.0 mA cm⁻² dendrite growth is so rapid and branched that short circuit of the cell may occur before full charge. It can be seen in Table 2 that as the mean current density increases the time it takes to reach m_{max} decreases, and the density of the dendrites also decreases. This is true for both PP and CC cases. As shown in Fig. 6, the deposition rate varies by charging protocol and i_m . The deposition rate exhibits non-linear behavior at higher applied potentials and in the initial phase of deposition. It is understood that current density should be proportional to deposition rate in a battery. Different deposition rates and total deposition times, as seen in Table 3 as well, indicate the current method of correlating current to applied potential is imperfect. However, correlating PP and CC deposition rate from the eBV-SPH model at the anode-electrolyte interface to current density is useful for the qualitative analysis of dendrite morphology and quantifying trends in performance across charging methods and parameters.

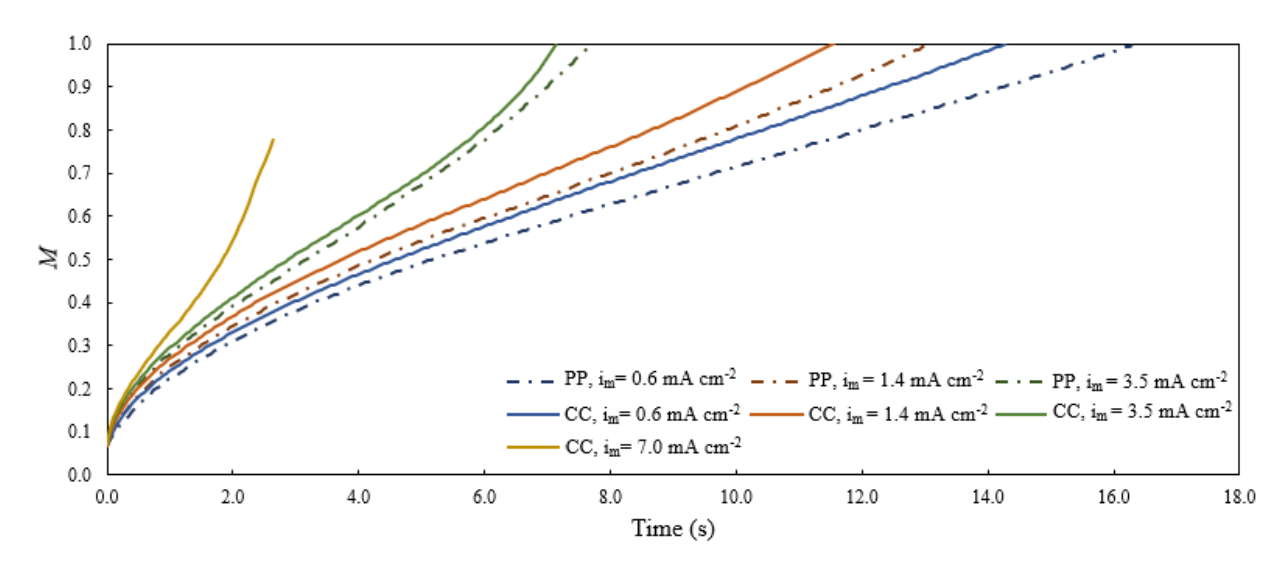


Figure 6: Li deposition (M) on the anode over total elapsed time.

A comparison of the PP and CC cases at the same mean current density is given in Table 3. For all cases, the PP charging protocol requires more time to reach M = 1.0. This means under

the same charging current density it will take longer to charge a battery using a PP protocol than a CC protocol. The deposition density is also compared for each case and presented in terms of both the mean current density and the charging current density of the PP protocol, which was held constant for all PP cases at $i_c = 7.0$ mA cm⁻². As expected, PP and specifically lower duty cycle values improved the density of Li deposition relative to the CC case at $i_c = 7.0$ mA cm⁻². The density ratio of PP and CC at the mean current values presented a reverse trend with smaller changes, ranging from 0.79 to 1.08 (Table 3). This indicates that the benefit of lowering the charging current (equal to i_m) in a CC protocol eventually surpasses the benefit of lowering the duty cycle in PP protocols. The mean current density, being representative of the overall charging in PP cases, is a more accurate marker of comparison between CC and PP. These results suggest that PP could still be utilized to improve dendrite growth and morphology. However, the optimization of PP protocols for superior electrodeposition or cycling performance should consider the performance of an alternative CC case at the mean current density.

Table 3: Comparison of deposition density and total charge time between PP and CC cases at the same mean current density. Note: subscripts on t and ρ correspond to the t and ρ values reported for PP and CC cases in Table 2.

Case	i _m [mA cm ⁻²]	$t_{\mathrm{PP}}/t_{\mathrm{CC}}$	ρ_{PP}/ρ_{CC} at i_m	ρ_{PP}/ρ_{CC} at i_c
PP-1/CC-1	0.6	1.14	0.79	3.24
PP-2/CC-2	1.4	1.13	1.05	2.38
PP-3/CC-3	3.5	1.07	1.08	1.42

Despite the similar deposition density values, the morphologies for PP and CC cases at identical mean charging current appear quite different (Fig. 7). Figure 7 shows the dendrite growth for both the CC cases (top row, Fig. 7a-d) and the PP cases (bottom row, Fig. 7e-g). Looking at CC, the higher the current density, the more branched the dendrite growth is (Fig. 7a-d). At lower applied current densities, the dendrites are shorter with fewer branches and thicker trunks (Fig. 7a). Note that Figure 7d can be considered the CC case or a PP case with duty cycle of 1.0. When the duty cycle is 1.0 (Fig.7d) the dendrites are thinly branched and there is significant vertical growth; while with a duty cycle is 0.09 (Fig. 7e) there is dense growth across the anode. The trend with duty cycle is comparable to the experimental results (Fig. 8) of Yang *et al.* [23]. Figure 8a ($i_c = 10 \text{ mA cm}^{-2}$) and Fig. 7d ($i_c = i_m = 7.0 \text{ mA cm}^{-2}$) which both have duty cycles of 1.0 display thin, branched dendrites due to CC charging at high current densities. Meanwhile, Fig. 7e ($i_m = 0.6 \text{ mA cm}^{-2}$; duty cycle = 0.09) and Fig. 8b ($i_m = 0.74 \text{ mA cm}^{-2}$; duty cycle = 0.07) both with a decreased duty cycle display denser dendrite morphologies and lower mean currents as the result of the PP

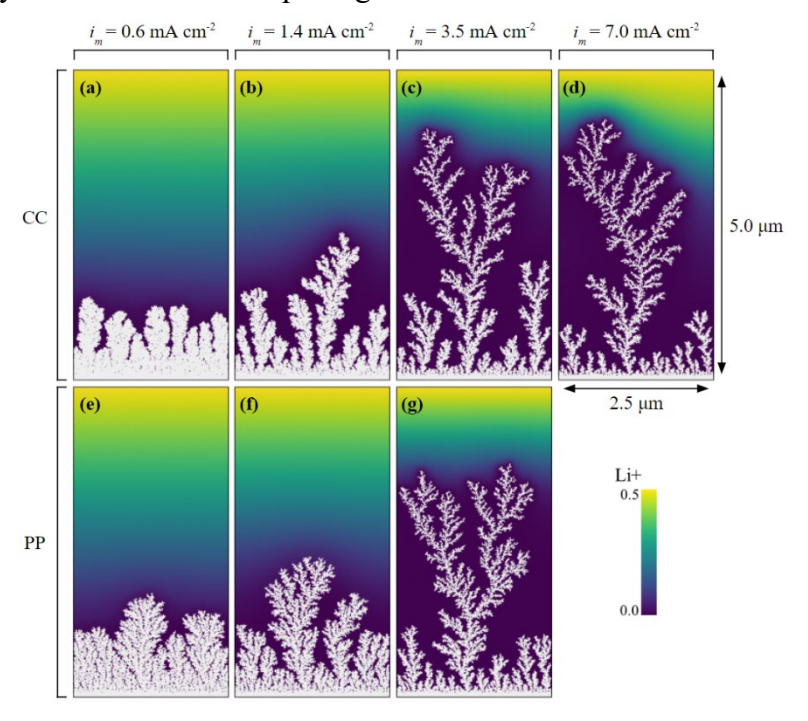


Figure 7: CC and PP charging to M = 1.0. CC cases C-1 through C-4 are shown in (a) through (d), and PP cases PP-1 through PP-3 are shown in (e) through (g). Details on each case are given in Table 2.

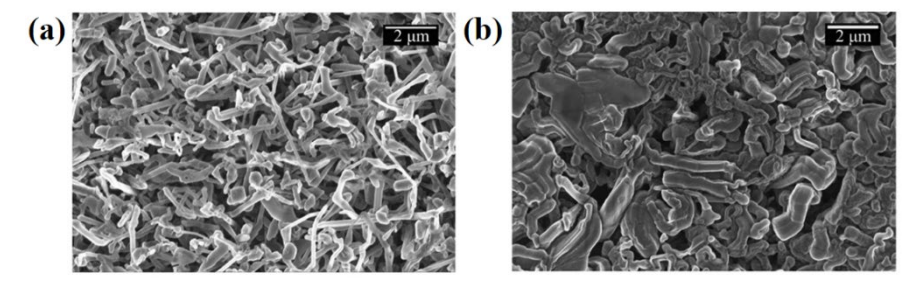


Figure 8: SEM images of Li electrodeposition with a modified button cell. Experimental results are for (a) CC charging at $i_c = 10$ mA cm⁻² and (b) PP charging at $i_c = 10$ mA cm⁻², D = 0.07, $i_m = 0.74$ mA cm⁻², and $f_{PP} = 185$ Hz. Adapted from Yang *et al.* [23].

charging protocol. Therefore, when comparing PP to CC using duty cycle as opposed to mean current, comparable results can be made between the simulation (Fig. 7) and the experimental results (Fig. 8).

Lower mean current densities, either from low duty cycles (PP-1 and Fig. 7e) or low constant charging currents (CC-1 and Fig. 7a) result in dense dendrite morphologies. For the CC protocol, the low current density allows for sufficient diffusion to occur and shifts the deposition towards a reaction limited regime. For PP, the short charging period limits the reduction reactions and Li⁺ depletion that can occur at the anode and dendrite tips. This creates a charging environment that is comparable to charging in the reaction limited regime. Likewise, the long relaxation period allows Li⁺ to replenish the electrolyte directly next to the dendrites where Li⁺ were rapidly consumed in the reduction reaction. This further shifts the deposition environment from a diffusion limited to reaction limited regime. Figure 9 shows the Li⁺ flux during charging and relaxation for case PP-3. When charging is occurring (Fig. 9a) the flux is negative (dark purple) near the dendrite and anode surface meaning that the Li⁺ are reacting at the surface and depleting the local ion concentration which pushes the system to a diffusion limited regime. When relaxation occurs (Fig. 9b) and there is no further growth of these dendrites, Li⁺ diffuse towards the dendrite tips and replenish the depleted regions. In contrast, during CC cases the flux at the tips of the anodes would remain negative throughout charging and the Li⁺ would be continuously consumed at the interface. The simulation results in Fig. 9 confirm the system is operating in a diffusion limited regime due to its high flux at the points of highest convexity (i.e. dendrite tips), which agrees with previous computational and experimental studies of similar systems [50,51].

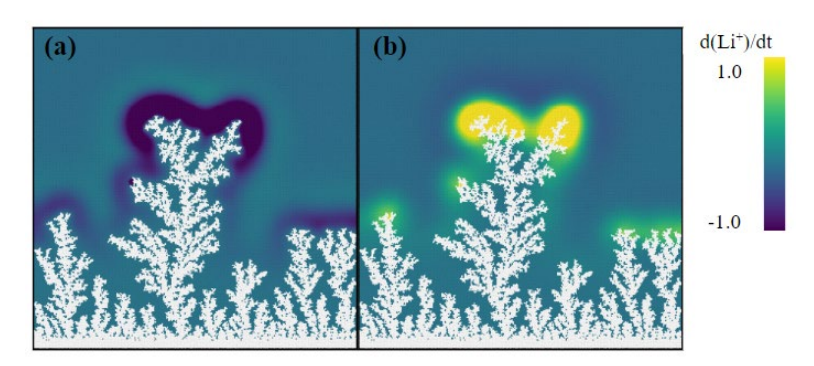


Figure 9: Li⁺ flux at start of the (a) charging period and (b) relaxation period for case PP-3.

When Li⁺ are replenished during the relaxation period, the Li⁺ concentration becomes more homogeneous resulting in more uniform Li deposition and fewer branched dendrites. This phenomenon can be seen in Fig. 10 where the effect of the charging and relaxation periods in PP are visually represented. In Fig. 10, the contours show Li⁺ concentration. Here it is seen that during charge (Fig. 10a) the Li⁺ concentration becomes depleted due to the Li plating on the anode surface, which results in a large concentration gradient. Following charging, when relaxation occurs (Fig. 10b), the concentration gradient decreases and the Li⁺ are replenished near the anode due to concentration driven diffusion in the electrolyte.

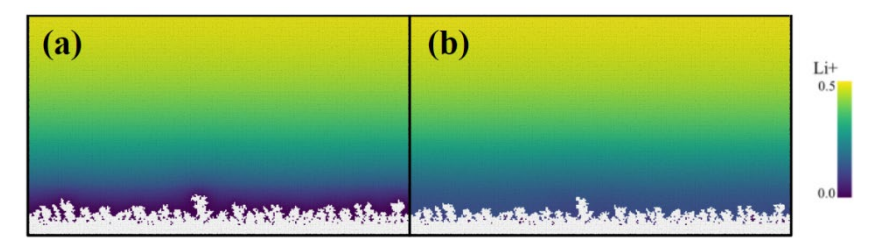


Figure 10: Concentration of Li⁺ ions at end of (a) charging period and (b) relaxation period for case PP-3.

5. Conclusions

The eBV-SPH model of dendrite growth was used to investigate the effect of PP charging protocols on dendrite growth and morphology. By reducing the concentration gradient during periods of low or no applied potential, PP allows diffusion to transport Li⁺ to the anode surface which reduces heterogeneous deposition. The relaxation period enables the use of a high current density during the charging period. Compared to standard CC charging at this high current density, PP has been shown to improve uniform Li deposition over a wide range of duty cycles, current densities, and pulse frequencies, resulting in favorable dendrite morphologies and superior cycling performance [23–26].

The use of computational methods allowed us to efficiently study the relevant physics occurring at the anode-electrolyte interface to gain a more robust understanding of the experimental results of previous groups [23,50,51]. While the model simulated the preferential growth of Li dendrites and visualizes dendrite morphology, Li⁺ concentrations, and Li⁺ flux, it does not directly model the SEI layer due to its complex nature. The growth of the SEI layer plays an important role in Li metal batteries and other alkali metals and its effect will be incorporated in future studies.

Through this study we were able to show that at lower duty cycles, short charge periods and long relaxation periods, Li electrodeposition forms dense, mossy dendrite growth due to Li⁺ diffusion towards the anode during the relaxation period resulting in a more uniform Li⁺ concentration gradient. The dendrite morphology qualitatively agreed with experimental results, where the morphology of the dendrites from CC at both the PP current and the identical mean current were visibly different from the PP dendrites.

Based on the simulation results from the eBV-SPH model, in conjunction with the experimental results reported by Yang et al. [23], it can be concluded that PP protocols increase the density of electrodeposited Li at high current densities and low duty cycles when compared with CC plating at the high current density (i_c) . If the benchmark charging method was instead CC plating at the identical mean current density (i_m) , the total charging times were comparable and PP protocols performed worse. Quantifying results against CC charging at the identical mean current proved to be a rigorous approach that demonstrated clear differences in morphology and reversed the trend in PP performance with lower duty cycles. Depositing m_{max} took between 1.07-1.14 times longer for PP than CC at identical mean currents [Table 3 and Fig. 6]. Meanwhile, the comparison of deposition densities at i_m showed a limit to the PP duty cycle parameter. As a result, it is recommended that future studies on PP protocols establish the mean current as the baseline of performance to determine the realistic performance gains of PP at various pulse frequencies, duty cycles, and current densities.

Acknowledgements

Financial support for this research is provided by the National Science Foundation through award numbers 1727316, and 2034154, the Boston University Undergraduate Research Opportunity Program, and the Hariri Institute for Computing and Computational Science and Engineering at Boston University through their Focused Research Program.

References

- [1] B. Liu, J.G. Zhang, W. Xu, Advancing Lithium Metal Batteries, Joule. 2 (2018) 833–845. https://doi.org/10.1016/J.JOULE.2018.03.008.
- [2] W. Xu, J. Wang, F. Ding, X. Chen, E. Nasybulin, Y. Zhang, J.G. Zhang, Lithium metal anodes for rechargeable batteries, Energy Environ. Sci. 7 (2014) 513–537. https://doi.org/10.1039/C3EE40795K.
- [3] J.M. Tarascon, M. Armand, Issues and challenges facing rechargeable lithium batteries, Nature. 414 (2001) 359–368. https://doi.org/10.1038/35104644.
- [4] J. Wang, B. Ge, H. Li, M. Yang, J. Wang, D. Liu, C. Fernandez, X. Chen, Q. Peng, Challenges and progresses of lithium-metal batteries, Chem. Eng. J. 420 (2021) 129739. https://doi.org/10.1016/j.cej.2021.129739.
- [5] C. Monroe, J. Newman, Dendrite Growth in Lithium/Polymer Systems, J. Electrochem. Soc. 150 (2003) A1377. https://doi.org/10.1149/1.1606686.
- [6] K. Nishikawa, T. Mori, T. Nishida, Y. Fukunaka, M. Rosso, Li dendrite growth and Li+ionic mass transfer phenomenon, J. Electroanal. Chem. 661 (2011) 84–89. https://doi.org/10.1016/J.JELECHEM.2011.06.035.
- [7] D. Lin, Y. Liu, Y. Cui, Reviving the lithium metal anode for high-energy batteries, Nat. Nanotechnol. 2017 123. 12 (2017) 194–206. https://doi.org/10.1038/nnano.2017.16.
- [8] E. Peled, The Electrochemical Behavior of Alkali and Alkaline Earth Metals in Nonaqueous Battery Systems—The Solid Electrolyte Interphase Model, J. Electrochem. Soc. 126 (1979) 2047–2051. https://doi.org/10.1149/1.2128859/XML.
- [9] A. Maraschky, R. Akolkar, Mechanism Explaining the Onset Time of Dendritic Lithium Electrodeposition via Considerations of the Li + Transport within the Solid Electrolyte Interphase , J. Electrochem. Soc. 165 (2018) D696–D703. https://doi.org/10.1149/2.0601814JES/XML.
- [10] K.N. Wood, E. Kazyak, A.F. Chadwick, K.-H. Chen, J.-G. Zhang, K. Thornton, N.P. Dasgupta, Dendrites and Pits: Untangling the Complex Behavior of Lithium Metal Anodes through Operando Video Microscopy, (2016). https://doi.org/10.1021/acscentsci.6b00260.
- [11] J.L. Barton, M.B. Ockris, The electrolytic growth of dendrites from ionic solutions, Proc. R. Soc. London. Ser. A. Math. Phys. Sci. 268 (1962) 485–505. https://doi.org/10.1098/RSPA.1962.0154.
- [12] X. Guan, A. Wang, S. Liu, G. Li, F. Liang, Y.-W. Yang, X. Liu, J. Luo, Controlling Nucleation in Lithium Metal Anodes, Small. 14 (2018) 1801423. https://doi.org/https://doi.org/10.1002/smll.201801423.
- [13] Y. Liu, X. Xu, M. Sadd, O.O. Kapitanova, V.A. Krivchenko, J. Ban, J. Wang, X. Jiao, Z. Song, J. Song, S. Xiong, A. Matic, Y. Liu, J. Ban, J. Wang, X. Jiao, Z. Song, J. Song, X. Xu, M. Sadd, S. Xiong, A. Matic, O.O. Kapitanova, V.A. Krivchenko, Insight into the Critical Role of Exchange Current Density on Electrodeposition Behavior of Lithium Metal,

- Adv. Sci. 8 (2021) 2003301. https://doi.org/10.1002/ADVS.202003301.
- [14] X. Xu, Y. Liu, J.Y. Hwang, O.O. Kapitanova, Z. Song, Y.K. Sun, A. Matic, S. Xiong, Role of Li-Ion Depletion on Electrode Surface: Underlying Mechanism for Electrodeposition Behavior of Lithium Metal Anode, Adv. Energy Mater. 10 (2020). https://doi.org/10.1002/AENM.202002390.
- [15] D. Sharon, P. Bennington, S.N. Patel, P.F. Nealey, Stabilizing dendritic electrodeposition by limiting spatial dimensions in nanostructured electrolytes, ACS Energy Lett. 5 (2020) 2889–2896. https://doi.org/10.1021/ACSENERGYLETT.0C01543.
- [16] K. Pan, L. Zhang, W. Qian, X. Wu, K. Dong, H. Zhang, S. Zhang, K. Pan, L. Zhang, W. Qian, X. Wu, K. Dong, H. Zhang, S. Zhang, A Flexible Ceramic/Polymer Hybrid Solid Electrolyte for Solid-State Lithium Metal Batteries, Adv. Mater. 32 (2020) 2000399. https://doi.org/10.1002/ADMA.202000399.
- [17] Y.J. Kim, H.S. Jin, D.H. Lee, J. Choi, W. Jo, H. Noh, J. Lee, H. Chu, H. Kwack, F. Ye, H. Lee, M.H. Ryou, H.T. Kim, Guided Lithium Deposition by Surface Micro-Patterning of Lithium-Metal Electrodes, ChemElectroChem. 5 (2018) 3169–3175. https://doi.org/10.1002/CELC.201800694.
- [18] A. Aryanfar, Y. Ghamlouche, W.A. Goddard, Real-time control of dendritic propagation in rechargeable batteries using adaptive pulse relaxation, J. Chem. Phys. 154 (2021) 194702. https://doi.org/10.1063/5.0042226.
- [19] M.Z. Mayers, J.W. Kaminski, T.F. Miller, Suppression of Dendrite Formation via Pulse Charging in Rechargeable Lithium Metal Batteries, J. Phys. Chem. C. 116 (2012) 26214–26221. https://doi.org/10.1021/jp309321w.
- [20] A. Aryanfar, D. Brooks, B. V. Merinov, W.A. Goddard, A.J. Colussi, M.R. Hoffmann, Dynamics of lithium dendrite growth and inhibition: Pulse charging experiments and monte carlo calculations, J. Phys. Chem. Lett. 5 (2014) 1721–1726. https://doi.org/10.1021/jz500207a.
- [21] A. Aryanfar, M.R. Hoffmann, W.A. Goddard, Finite-pulse waves for efficient suppression of evolving mesoscale dendrites in rechargeable batteries, Phys. Rev. E. 100 (2019). https://doi.org/10.1103/PHYSREVE.100.042801.
- [22] A. Aryanfar, D.J. Brooks, W.A. Goddard, Theoretical pulse charge for the optimal inhibition of growing dendrites, MRS Adv. 3 (2018) 1201–1207. https://doi.org/10.1557/ADV.2018.97.
- [23] H. Yang, E.O. Fey, B.D. Trimm, N. Dimitrov, M.S. Whittingham, Effects of Pulse Plating on lithium electrodeposition, morphology and cycling efficiency, J. Power Sources. 272 (2014) 900–908. https://doi.org/10.1016/j.jpowsour.2014.09.026.
- [24] Z. Zhang, Z.L. Wang, X. Lu, Suppressing Lithium Dendrite Growth via Sinusoidal Ripple Current Produced by Triboelectric Nanogenerators, Adv. Energy Mater. 9 (2019) 1900487n/a. https://doi.org/10.1002/aenm.201900487.
- [25] Q. Li, S. Tan, L. Li, Y. Lu, Y. He, Understanding the molecular mechanism of pulse current charging for stable lithium-metal batteries, 2017. http://advances.sciencemag.org/.
- [26] G. García, S. Dieckhöfer, W. Schuhmann, E. Ventosa, Exceeding 6500 cycles for LiFePO4/Li metal batteries through understanding pulsed charging protocols, J. Mater. Chem. A. 6 (2018) 4746–4751. https://doi.org/10.1039/C8TA00962G.
- [27] M.S. Chandrasekar, M. Pushpavanam, Pulse and pulse reverse plating—Conceptual, advantages and applications, Electrochim. Acta. 53 (2008) 3313–3322. https://doi.org/10.1016/J.ELECTACTA.2007.11.054.

- [28] X. Huang, Y. Li, A.B. Acharya, X. Sui, J. Meng, R. Teodorescu, D.I. Stroe, A review of pulsed current technique for lithium-ion batteries, Energies. 13 (2020). https://doi.org/10.3390/EN13102458.
- [29] A. Aryanfar, Y. Ghamlouche, W.A. Goddard, Pulse Reverse Protocol for efficient suppression of dendritic micro-structures in rechargeable batteries, Electrochim. Acta. 367 (2021). https://doi.org/10.1016/j.electacta.2020.137469.
- [30] M.S. Chandrasekar, M. Pushpavanam, Pulse and pulse reverse plating-Conceptual, advantages and applications, Electrochim. Acta. 53 (2008) 3313–3322. https://doi.org/10.1016/J.ELECTACTA.2007.11.054.
- [31] I.W. Seong, C.H. Hong, B.K. Kim, W.Y. Yoon, The effects of current density and amount of discharge on dendrite formation in the lithium powder anode electrode, J. Power Sources. 178 (2008) 769–773. https://doi.org/10.1016/j.jpowsour.2007.12.062.
- [32] A.W. Abboud, E.J. Dufek, B. Liaw, Communication—Implications of Local Current Density Variations on Lithium Plating Affected by Cathode Particle Size, J. Electrochem. Soc. 166 (2019) A667–A669. https://doi.org/10.1149/2.0711904JES.
- [33] H. Sano, H. Sakaebe, H. Senoh, H. Matsumoto, Effect of Current Density on Morphology of Lithium Electrodeposited in Ionic Liquid-Based Electrolytes, J. Electrochem. Soc. 161 (2014) A1236–A1240. https://doi.org/10.1149/2.0331409JES.
- [34] P. Keil, A. Jossen, Charging protocols for lithium-ion batteries and their impact on cycle life—An experimental study with different 18650 high-power cells, J. Energy Storage. 6 (2016) 125–141. https://doi.org/10.1016/J.EST.2016.02.005.
- [35] A. Maraschky, R. Akolkar, Pulsed Current Plating Does Not Improve Microscale Current Distribution Uniformity Compared to Direct Current Plating at Equivalent Time-Averaged Plating Rates, J. Electrochem. Soc. 168 (2021) 062507. https://doi.org/10.1149/1945-7111/AC07C4.
- [36] R.A. Gingold, J.J. Monaghan, Smoothed particle hydrodynamics: theory and application to non-spherical stars, Mon. Not. R. Astron. Soc. 181 (1977) 375–389. https://doi.org/10.1093/MNRAS/181.3.375.
- [37] J.J. Monaghan, Smoothed particle hydrodynamics, Reports Prog. Phys. 68 (2005) 1703–1759. https://doi.org/10.1088/0034-4885/68/8/R01.
- [38] J.J. Monaghan, Smoothed particle hydrodynamics and its diverse applications, Annu. Rev. Fluid Mech. 44 (2011) 323–346. https://doi.org/10.1146/ANNUREV-FLUID-120710-101220.
- [39] A. Cannon, J.G. McDaniel, E. Ryan, Smoothed particle hydrodynamics modeling of electrodeposition and dendritic growth under migration- and diffusion-controlled mass transport, Comput. Mater. Sci. Unpublished (2021).
- [40] J. Tan, A. Cannon, E. Ryan, Simulating dendrite growth in lithium batteries under cycling conditions, J. Power Sources. 463 (2020). https://doi.org/10.1016/j.jpowsour.2020.228187.
- [41] M. Morey, J. Loftus, A. Cannon, E. Ryan, Interfacial studies on the effects of patterned anodes for guided lithium deposition in lithium metal batteries, J. Chem. Phys. 156 (2022) 14703. https://doi.org/10.1063/5.0073358.
- [42] A.P. Thompson, H.M. Aktulga, R. Berger, D.S. Bolintineanu, W.M. Brown, P.S. Crozier, P.J. in 't Veld, A. Kohlmeyer, S.G. Moore, T.D. Nguyen, R. Shan, M.J. Stevens, J. Tranchida, C. Trott, S.J. Plimpton, LAMMPS a flexible simulation tool for particle-based materials modeling at the atomic, meso, and continuum scales, Comput. Phys. Commun. 271 (2022) 108171. https://doi.org/10.1016/J.CPC.2021.108171.

- [43] J. Tan, E.M. Ryan, Computational study of electro-convection effects on dendrite growth in batteries, J. Power Sources. 323 (2016) 67–77. https://doi.org/10.1016/j.jpowsour.2016.05.012.
- [44] S. Rajendran, Z. Tang, A. George, A. Cannon, C. Neumann, A. Sawas, E. Ryan, A. Turchanin, L.M.R. Arava, Inhibition of Lithium Dendrite Formation in Lithium Metal Batteries via Regulated Cation Transport through Ultrathin Sub-Nanometer Porous Carbon Nanomembranes (Adv. Energy Mater. 29/2021), Adv. Energy Mater. 11 (2021) 2170114. https://doi.org/10.1002/AENM.202170114.
- [45] J. Tan, A.M. Tartakovsky, K. Ferris, E.M. Ryan, Investigating the Effects of Anisotropic Mass Transport on Dendrite Growth in High Energy Density Lithium Batteries, J. Electrochem. Soc. 163 (2016) A318–A327. https://doi.org/10.1149/2.0951602JES.
- [46] J.S. Newman, K.E. Thomas-Alyea, Electrochemical systems, 3rd edition, Wiley-Interscience, 2004.
- [47] B. Lu, Y. Song, Q. Zhang, J. Pan, Y.T. Cheng, J. Zhang, Voltage hysteresis of lithium ion batteries caused by mechanical stress, Phys. Chem. Chem. Phys. 18 (2016) 4721–4727. https://doi.org/10.1039/C5CP06179B.
- [48] A.M. Tartakovsky, P. Meakin, T.D. Scheibe, R.M. Eichler West, Simulations of reactive transport and precipitation with smoothed particle hydrodynamics, J. Comput. Phys. 222 (2007) 654–672. https://doi.org/10.1016/J.JCP.2006.08.013.
- [49] I.J. Schoenberg, Contributions to the Problem of Approximation of Equidistant Data by Analytic Functions, in: C. de Boor (Ed.), I. J. Schoenb. Sel. Pap., Birkhäuser Boston, Boston, MA, 1988: pp. 58–87. https://doi.org/10.1007/978-1-4899-0433-1_2.
- [50] H.H. Chang, Computer simulations of isolated conductors in electrostatic equilibrium, Phys. Rev. E Stat. Nonlinear, Soft Matter Phys. 78 (2008). https://doi.org/10.1103/PHYSREVE.78.056704.
- [51] Q. Li, B. Quan, W. Li, J. Lu, J. Zheng, X. Yu, J. Li, H. Li, Electro-plating and stripping behavior on lithium metal electrode with ordered three-dimensional structure, Nano Energy. 45 (2018) 463–470. https://doi.org/10.1016/J.NANOEN.2018.01.019.